EVALUATION OF TEMPERATURE EFFECTS ON PASSIVE ACOUSTIC DAMPERS WITH A FREQUENCY-DOMAIN LINEARIZED NAVIER-STOKES EQUATIONS SOLVER

Jonathan Tournadre and Wim Desmet

KU Leuven, Dept. of Mechanical Engineering, Celestijnenlaan 300B, 3001 Leuven, Belgium
email: jonathan.tournadre@kuleuven.be

Paula Martínez-Lera

Siemens Industry Software, Researchpark 1237, Interleuvenlaan 68, 3001 Leuven, Belgium

The present work investigates numerically the temperature effects on the behavior of Helmholtz resonators with the help of the Linearized Navier-Stokes equations. The equations are solved in the frequency domain using a high-order Finite Element Method. The numerical method is applied to the case of Helmholtz resonators with given temperature profiles inside their neck and cavity. The obtained impedances are compared to an existing model for the equivalent cold flow case with modified fluid properties (density, viscosity and speed of sound) to assess the quality of this approximation. Simulations with the complete set of equations, accounting for viscous and thermal effects in the energy equation, are compared to simulations under the isentropic assumption in terms of the different dissipation mechanisms and global absorption coefficient. It is found that the isentropic assumption is not suitable at low Helmholtz number, and that the discrepancy increases with growing temperature gradient inside the resonator neck.

1. Introduction

Perforates of small dimensions, coupled with a backing volume, are commonly used as acoustic dampers for both noise emission reduction and control of combustion instabilities. For some of those applications, like inside the combustion chamber of a turbine or for hot stream acoustic liners in an engine exhaust duct, perforates can be subjected to a wide range of temperatures and to significant temperature gradients. Even if research on impedance modeling of perforates has been going for several decades, most of the existing impedance models have been derived at ambient temperature. This is a consequence of the difficulties to perform pressure measurements under hot conditions, especially when flow is present. Some experimental works have been done under non-isothermal conditions, both in the absence of mean flow [1] and in presence of a hot grazing flow [2, 3]. The influence of non-isopycnic conditions on the length corrections at the resonator neck has also been investigated with cold-flow experiments with the mixing of different gases [4].

This paper investigates numerically the high temperature and temperature gradient effects on the acoustic behavior of a Helmholtz resonator in absence of mean flow. For this purpose, the complete set of the non-isentropic Linearized Navier-Stokes (LNS) equations are solved here in the frequency domain. By accounting for the coupling of acoustic, vorticity and entropy modes, the simulations allow to quantify each of the physical source/sink terms responsible for the acoustic damping. An estimation of the impedance including temperature effects can be obtained by scaling the impedance resulting from measurements under cold conditions with modified fluid properties (density, viscosity

and speed of sound). This scaling is investigated, along with the impact of temperature gradients in the resonator neck. Additionally, results from both isentropic and non-isentropic sets of equations are compared to assess in detail the accuracy of isothermal non-isopycnic approaches.

This paper describes first the governing equations and the applied numerical technique in Sec. 2.1 and Sec. 2.2. The method to evaluate the different dissipation mechanisms on an acoustic perturbation is described in Sec. 2.3. The case of a Helmholtz resonator at different temperatures is presented in Sec. 3, both for homogeneous temperature field and in presence of a linear temperature profile.

2.   Computational method and evaluation of the dissipation mechanisms

2.1   Linearized Navier-Stokes equations for non-isentropic conditions

The linear regime of an orifice under non-isothermal conditions can be simulated by the perturbed version of the full compressible Navier-Stokes equations. The traditional approach is to consider any instantaneous variable $q(\mathbf{x}, t)$ as the sum of a variable describing the time averaged quantity $q_0(\mathbf{x})$ and a relatively smaller harmonic perturbation $q'(\mathbf{x}, t)$. Applying such decomposition, the linearized Navier-Stokes equations under non-isentropic conditions can be written as:

$$
\left\{
\begin{aligned}
&\textbf{Continuity:} \quad && \frac{\partial \rho'}{\partial t} + \frac{\partial(\rho_0 u'_r + \rho' u_{0r})}{\partial x_r} = 0\,, && \text{(1a)} \\[2mm]
&\textbf{Momentum:} \quad && \frac{\partial \rho_0 u'_s}{\partial t} + \frac{\partial \rho_0 u'_s u_{0r}}{\partial x_r} + \frac{\partial p'}{\partial x_s} + (\rho_0 u'_r + \rho' u_{0r})\frac{\partial u_{0s}}{\partial x_r} - \frac{\partial \tau'_{sr}}{\partial x_r} = 0\,, && \text{(1b)} \\[2mm]
&\textbf{Energy:} \quad && \frac{\partial p'}{\partial t} + u_{0r}\frac{\partial p'}{\partial x_r} + u'_r\frac{\partial p_0}{\partial x_r} + \gamma p_0\frac{\partial u'_r}{\partial x_r} + \gamma p'\frac{\partial u_{0r}}{\partial x_r} = && \\[2mm]
& && \qquad (\gamma - 1)\left[\frac{\partial}{\partial x_r}(\lambda_t \frac{\partial T'}{\partial x_r}) + \tau_{0rs}\frac{\partial u'_r}{\partial x_s} + \tau'_{rs}\frac{\partial u_{0r}}{\partial x_s} + \dot{q}'_V\right]\,, && \text{(1c)}
\end{aligned}
\right.
$$

with

$$
\tau'_{sr} = \mu\left(\frac{\partial u'_s}{\partial x_r} + \frac{\partial u'_r}{\partial x_s} - \frac{2}{3}\frac{\partial u'_k}{\partial x_k}\delta_{rs}\right)\,, \qquad s' = C_p\frac{T'}{T_0} - R_0\frac{p'}{p_0}\,, \quad \text{and} \quad T' = T_0\left(\frac{p'}{p_0} - \frac{\rho'}{\rho_0}\right)\,,
$$

where ρ, $\mathbf{u}$, p, T, and s are the density, velocity, pressure, temperature, and entropy fields. μ is the dynamic viscosity, λ_t the thermal conductivity, C_p the heat capacity at constant pressure, R_0 the specific gas constant, δ the Kronecker delta function and τ_{sr} is the viscous stress tensor. $\dot{q}'_V$ represents internal heat sources, but in this work we assume $\dot{q}'_V = 0$. As temperature gradients are present in the investigated cases, the local values of the fluid viscosity as well as the other mean flow properties are considered. Under the assumption of isentropic conditions, the set of equations is simply obtained from Eq. (1) by taking the right-hand side of the energy equation (1c) equal to zero.

2.2   High-oder Finite Element Method implementation

The set of the Linearized Navier-Stokes equations Eq. (1), for both isentropic and non-isentropic versions, are solved using a high-order FEM (p-FEM) frequency domain solver [5, 6]. A set of Lobatto shape functions is used here for the expansion of each field variable. The perturbation quantities are assumed to be harmonic time dependent variables that can be written as $q'(\mathbf{x}, t) = \hat{q}(\mathbf{x})\mathrm{e}^{+\mathrm{j}\omega t}$, where $\hat{q}$ is a complex quantity and ω is the angular frequency.

All walls of the physical domain are assumed impermeable and acoustically rigid. One can apply wall slip boundary conditions ($\mathbf{u}'.\mathbf{n} = 0$) where the acoustic boundary layer is expected to play no significant role and no-slip wall boundary condition otherwise ($\mathbf{u}' = \mathbf{0}$). An additional condition on the temperature field is required for the non-isentropic problems, on the boundaries where the thermal

boundary layer is resolved. Walls are assumed here to have a constant temperature T_0, meaning that the temperature fluctuations vanish, i.e. $T' = 0$ (Dirichlet type). From the linearized state equation, this leads to $p' - \rho' p_0/\rho_0 = 0$. Non-reflecting characteristic boundary conditions are further applied on the truncated boundaries of the domain, in order to avoid outgoing waves to be artificially reflected back inside the physical domain.

2.3   Post-processing of the acoustic energy dissipation mechanisms

Myers [7] derived an exact equation governing the transport of energy associated with disturbance in an arbitrary steady flow. The generalized formulation of this corollary has been obtained by perturbation expansion of the energy conservation equation of fluid and is valid at any nth order of magnitude of the unsteady disturbance, for $n \in \mathbb{N}$. For order $n = 1$, it yields for the energy of the perturbed field:

$$\frac{\partial \mathcal{E}'}{\partial t} + \frac{\partial \mathcal{W}'_i}{\partial x_i} = \mathcal{D}', \tag{2}$$

where $\mathcal{E}'$ defines the first-order disturbance energy density, $\mathcal{W}'$ is the first-order energy flux vector, and $\mathcal{D}'$ represents the source/sink term for the first-order energy. $\mathcal{D}'$ describes the volumetric rate at which the first-order disturbance energy is being dissipated. This equation, which contains only first-order perturbation quantities, satisfies the principle of total fluid energy conservation at the second order. The disturbance energy density $\mathcal{E}'$ is further given by:

$$\mathcal{E}' = \frac{p'^2}{2\rho_0 c_0} + \frac{1}{2}\rho_0 \mathbf{u}'^2 + \rho' \mathbf{u_0} \cdot \mathbf{u}' + \frac{\rho_0 T_0 s'^2}{2 C_p}. \tag{3}$$

The source terms $\mathcal{D}'$ can be expressed as the sum of the contributions of each of the physical mechanisms involved in the growth/decrease of the perturbed energy inside the control volume. We distinguish here between mechanisms related to the vorticity $\mathcal{D}'_v$, entropy $\mathcal{D}'_s$, viscous diffusion $\mathcal{D}'_\mu$, internal heat source $\mathcal{D}'_q$, and thermal diffusion $\mathcal{D}'_t$. These terms can be expressed as:

$$\mathcal{D}'_v = \rho_0 \mathbf{u_0} \cdot (\boldsymbol{\Omega}' \times \mathbf{u}') + \rho' \mathbf{u}' \cdot (\boldsymbol{\Omega_0} \times \mathbf{u_0}), \qquad \mathcal{D}'_s = -s' \mathbf{m}' \cdot \nabla T_0 + s' \rho_0 \mathbf{u_0} \cdot \nabla T',$$

$$\mathcal{D}'_\mu = -\left(\frac{\tau_{ij}}{\rho}\right)' \frac{\partial m'_j}{\partial x_i} + m'_j \left(\frac{\tau_{ij}}{\rho^2} \frac{\partial \rho}{\partial x_i}\right)', \qquad \mathcal{D}'_q = \frac{T'}{T_0}\left(\dot{q}'_V - T' \dot{q}_{V0}\right), \text{ and} \tag{4}$$

$$\mathcal{D}'_t = \left(\frac{-\lambda_t \nabla T}{T}\right)' \cdot \nabla T' - T'\left(\frac{-\lambda_t \nabla T \cdot \nabla T}{T^2}\right)',$$

where $m' = (\rho_0 \mathbf{u}' + \rho' \mathbf{u_o})$ is the mass flux vector perturbation and $\boldsymbol{\Omega}$ the vorticity $\nabla \times \mathbf{u}$. For the present case, where $\mathbf{u_0} = \mathbf{0}$ and $\dot{q}'_V = \dot{q}_{V0} = 0$, it follows that $\mathcal{D}'_v = 0$ and $\mathcal{D}'_q = 0$. The component in the i-direction of the first-order disturbance energy flux vector $\mathcal{W}'$ is defined as:

$$\mathcal{W}'_i = m'_i\left(\frac{p'}{p_0} + \mathbf{u_0} \cdot \mathbf{u}'\right) - m'_j\left(\frac{\tau_{ij}}{\rho}\right)' + \rho_0 u_{0i} T' s' + \frac{T'}{T_0}\left(-\lambda_t \frac{\partial T'}{\partial x_i} + \frac{\lambda_t}{T_0}\frac{\partial T_0}{\partial x_i} T'\right). \tag{5}$$

The first term of the right-hand side in Eq. (5) corresponds to the perturbed acoustic energy flux, whereas the second gives the viscous stress power and the two last ones represent entropy and thermal effects.

Similarly to [8], but accounting here for the visco-thermal losses, the time-average of the perturbed energy equation defined in Eq. (2) is integrated over the volume V with surface S and unity normal vector $\mathbf{n}$ to describe the overall energy balance. It gives:

$$\int_V \overline{\frac{\partial \mathcal{E}'}{\partial t}}\, \mathrm{d}V + \int_S \overline{\mathcal{W}'} \cdot \mathbf{n}\, \mathrm{d}S = \int_V \overline{\mathcal{D}'}\, \mathrm{d}V \qquad \Leftrightarrow \qquad \mathbb{E}' + \mathbb{W}' = \mathbb{D}'. \tag{6}$$

The integral terms in the energy balance are referred to here as $\mathbb{E}'$, $\mathbb{W}'$, and $\mathbb{D}'$. In the following, the integration volume V represents the complete numerical domain and the integrals defined in Eq. (6)

are computed in a post-processing step after solving the initial problem described in Sections 2.1 and 2.2. Due to the choice of harmonic perturbation fields, the first term in Eq. 6 is equal to zero, i.e. $\mathbb{E}' = 0$. The same subscript conventions are kept for the source/sink integral terms $\mathbb{D}'_\bullet$ to distinguish between the different types of dissipation mechanisms.

3. Temperature effects on the acoustic behavior of Helmholtz resonators

The configuration of a 2-D Helmholtz resonator with orifice diameter $d_o = 1.5\,\text{mm}$, orifice thickness $l_o = 1\,\text{mm}$, back cavity length $l_{\text{cav}} = 17.5\,\text{mm}$ and diameter $d_{\text{cav}} = 10\,\text{mm}$ is investigated at three different temperatures, $T_0 \in \{300\,\text{K}, 500\,\text{K}, 700\,\text{K}\}$. The resonator (see Fig. 1) is placed at the extremity of an impedance tube of length $l_{\text{duct}} = 500\,\text{mm}$ and diameter $d_{\text{duct}} = 40\,\text{mm}$, in which a multi-microphone system identification technique is performed to extract the resonator reflection coefficient R and acoustic impedance z.

3.1 High temperature resonator without temperature gradient

As the temperature increases, the resonance frequency shifts towards higher values, as illustrated in Fig. 2. This shift originates from the increase in the speed of sound inside the backing volume, whereas the cavity dimensions stay the same. It is captured correctly by the numerical LNS simulations. This change in the wavenumber can be filtered out by representing the results in terms of the Helmholtz number He, defined here as $He = k_0 d_o$. Only temperature effects on the visco-thermal losses remain then.
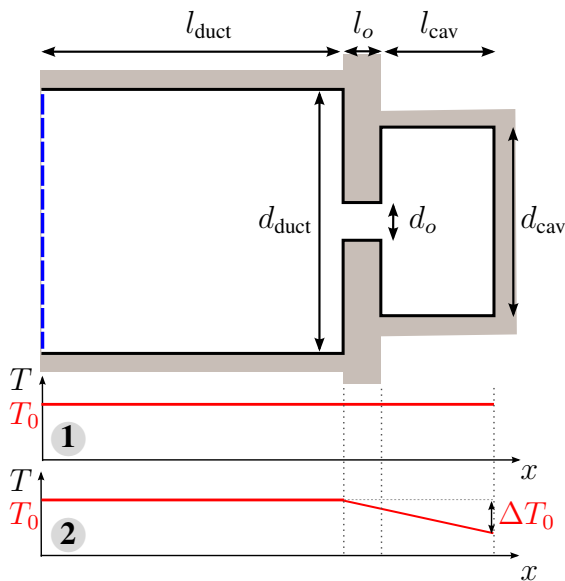

Figure 1: Helmholtz resonator configuration and temperature profiles: 1) Homogeneous, 2) Linear profile.
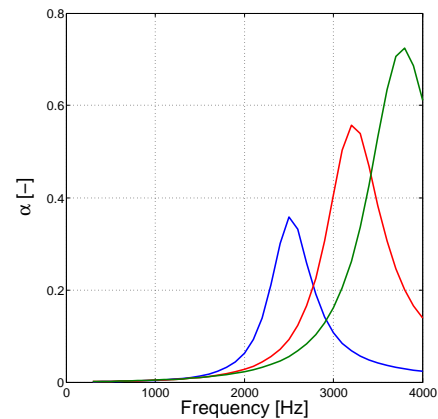

Figure 2: Absorption coefficient α in function of the frequency at three different temperatures: results at $T_0 = 300\,\text{K}$ (——), $T_0 = 500\,\text{K}$ (——), and $T_0 = 700\,\text{K}$ (——) from the non-isentropic LNS solver.

Figure 3(a) shows the impact of the temperature on the reflection coefficient. From the reflection coefficient curves, it can be seen that the visco-thermal losses rise with increasing temperature. A slight shift towards lower Helmholtz numbers can be observed for the resonance peak as well. This shift appears to be larger between $T_0 = 500\,\text{K}$ and $700\,\text{K}$ than between $T_0 = 300\,\text{K}$ and $500\,\text{K}$. By comparing the results from the isentropic LNS p-FEM solver and the ones coming from the complete set of non-isentropic LNS equations, one can see that only very little additional thermal dissipation is
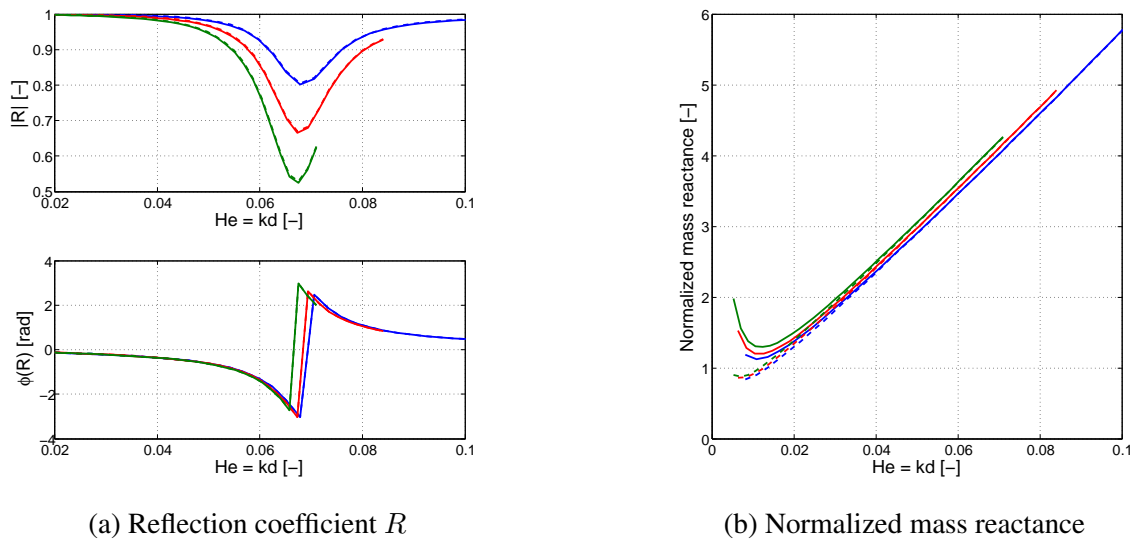
(a) Reflection coefficient R

(b) Normalized mass reactance

Figure 3: Acoustic behavior of the studied Helmholtz resonator in different homogeneous temperature environments: results at $T_0 = 300\,\mathrm{K}$ (——), $T_0 = 500\,\mathrm{K}$ (——), and $T_0 = 700\,\mathrm{K}$ (——) from the isentropic LNS solver (- - -) and from the non-isentropic one (——).
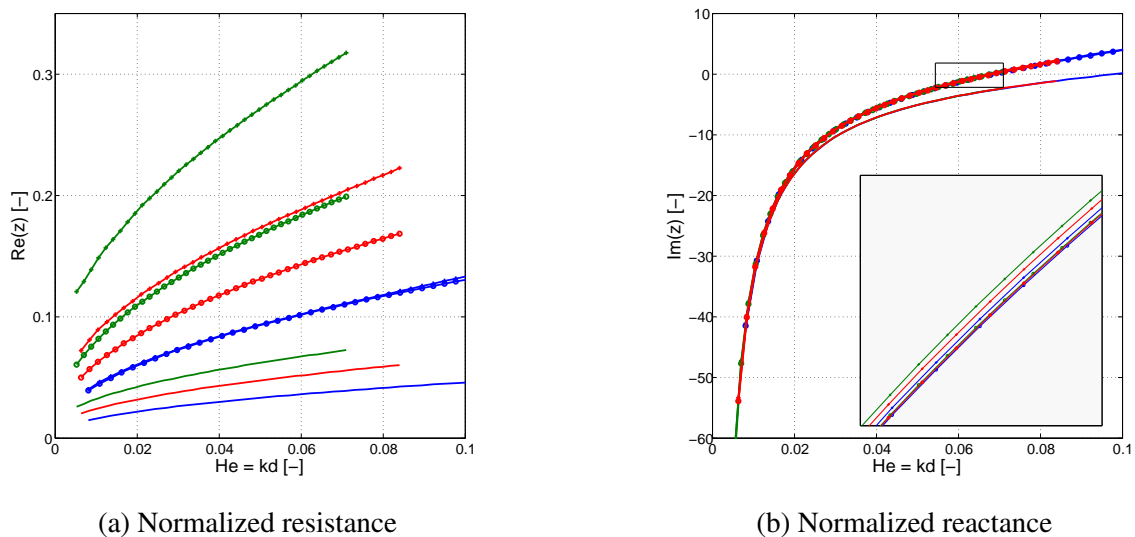
(a) Normalized resistance

(b) Normalized reactance

Figure 4: Normalized resistance (left) and reactance (right) of the investigated Helmholtz resonator at three temperature levels - $T_0 = 300\,\mathrm{K}$ (——), $T_0 = 500\,\mathrm{K}$ (——), and $T_0 = 700\,\mathrm{K}$ (——) - obtained from Maa/Allam [9, 10] model discarding end-corrections (——), from complete Maa/Allam model scaled with fluid properties (—∘—) and computed from p-FEM LNS solver (—+—).

found by resolving the thermal boundary layer inside the resonator neck. This fact holds for the three investigated temperatures.

The normalized mass reactance, representing the end-correction effects for the resonator neck, is shown in Fig. 3(b). An increase in this quantity is found for rising temperature and can be related to the shift towards lower He values for the reflection peak. The slope of the curves is nearly the same for the higher part of the investigated He range. The results given by the two solvers are also here very close, with discrepancies in the predicted normalized mass reactance appearing only for the very low He limit (for $He < 0.025$). Additional thermal losses appear to increase the end-corrections for very small He.

Figure 4 shows the computed impedance values for the studied Helmholtz resonator compared to the impedance values predicted with a semi-empirical model scaled with the fluid properties (ρ_0, μ and

c_0) according to the temperature. As the present simulations are carried out for a 2-D geometry and end-corrections for 2-D models are not easily available in the literature, the semi-empirical impedance model used here is the one given by Maa [9] and Allam [10] for a slit-shaped orifice. This model defines the normalized resistance and reactance in the linear regime as

$$\text{Re}(z) = \text{Re}\left(\frac{j\omega t_o}{\sigma c_0}\left[1 - \frac{\tanh\left(\kappa\sqrt{j}\right)}{\kappa\sqrt{j}}\right]^{-1}\right) + \frac{\alpha R_s}{\sigma \rho_0 c_0} + \frac{\sigma_{\text{BC}}\alpha R_s}{\sigma \rho_0 c_0}, \tag{7}$$

$$\text{Im}(z) = \text{Im}\left(\frac{j\omega t_o}{\sigma c_0}\left[1 - \frac{\tanh\left(\kappa\sqrt{j}\right)}{\kappa\sqrt{j}}\right]^{-1}\right) + 0.5\,\frac{\delta_s\omega}{\sigma c_0} + 0.5\,\frac{\sigma_{\text{BC}}\delta_s\omega}{\sigma c_0}. \tag{8}$$

Here, the dimensionless shear number κ relates the orifice radius to the viscous boundary layer thickness and is defined as $\kappa = d_o\sqrt{\omega\rho_0/(4\mu)}$. Note that the model is expressed here for the case where the back cavity diameter differs from the duct diameter in which the resonator is placed, as it is the case in the present work. σ represents the open area ratio on the side of the impedance duct, whereas σ_{BC} is the one on the backing volume side. The end-correction parameter α for the resistance and the one for the reactive part δ_s, which depends on the supposed third dimension of the orifice l_s through an equivalent diameter $d_{\text{eq}} = 2\sqrt{d_o l_s/\pi}$, have been fitted to match the numerical results for the case at $T_0 = 300\,\text{K}$. This case is taken here as reference, as such model has been first developed for ambient conditions. The values found for these parameters are: $\alpha = 2.25\,[-]$, $\delta_s = 0.85\,d_{\text{eq}}$ with $l_s = 0.01\,\text{m}$.

The basic scaling of the model with respect to the fluid properties appears to deliver very good results for the reactance (see Fig. 4(b)). A close-up view of the curves reveals however a slight increase in the inertia in the numerical results, which is not captured at all by the semi-empirical model. Considering the wide range of temperature condition in this study, it is nevertheless expected that this discrepancy is not of importance for practical applications. Concerning the resistive part, the applied scaling is found to be less suitable. Even if the trend of increasing resistance with rising temperature is found similar between the model and the numerical predictions, the scaling of the semi-empirical model is unable to capture correctly the amount of additional visco-thermal losses due to higher temperature. The end-corrections in terms of visco-thermal damping do not only depend on the fluid properties, but have an extra dependency on the temperature. The higher the temperature, the more inaccurate the model is. The experimental work done by Elnady *et al.* [1] leads to similar conclusions, even if in their case some nonlinear effects and the impact of a small temperature gradient through the orifice might be present as well. In their study, the impedance model by Elnady tends nonetheless to overestimate the visco-thermal losses.

3.2   High temperature resonator with temperature gradient

For the case with $T_0 = 700\,\text{K}$, an arbitrary linear temperature profile is imposed, defined between the resonator face sheet at T_0 and the temperature at the backing wall $T_w = T_0 - \Delta T_0$, for $\Delta T_0 \in [0\,\text{K} - 500\,\text{K}]$, see Fig. 1. It provides a maximal temperature gradient of $21.6\,\text{K}$ through the orifice.

Figures 5(a,b,c) show for different temperature conditions the distinct terms of the perturbed energy balance in Eq. (4), displayed as $10\log\left(|\mathbb{D}'_\bullet|^2\right)$. Results are represented in function of the frequency, as it is not evident yet which relevant temperature is to be considered for the definition of He in presence of a temperature gradient. First, we can see that in all cases the energy balance given in Eq. (2) is satisfied, with the relation $\mathbb{W}' = \mathbb{D}'$ verified over the entire frequency range of this study. The dissipation terms are maximal at the resonance frequency (around $f = 3700\,\text{Hz}$), as the amplitudes of the velocity and temperature fluctuations are maximal at the resonance. For the homogeneous temperature case, i.e. Fig. 5(a), the viscous losses are clearly the predominant ones. Thermal losses are quantitatively not varying significantly through the frequency range and are of importance only at low frequencies. The dissipation term related to entropy is, as expected, close to zero in the absent of temperature gradient.

(a) $T_0 = 700\,\mathrm{K}$ and $\Delta T_0 = 0\,\mathrm{K}$

(b) $T_0 = 700\,\mathrm{K}$ and $\Delta T_0 = 100\,\mathrm{K}$

(c) $T_0 = 700\,\mathrm{K}$ and $\Delta T_0 = 500\,\mathrm{K}$
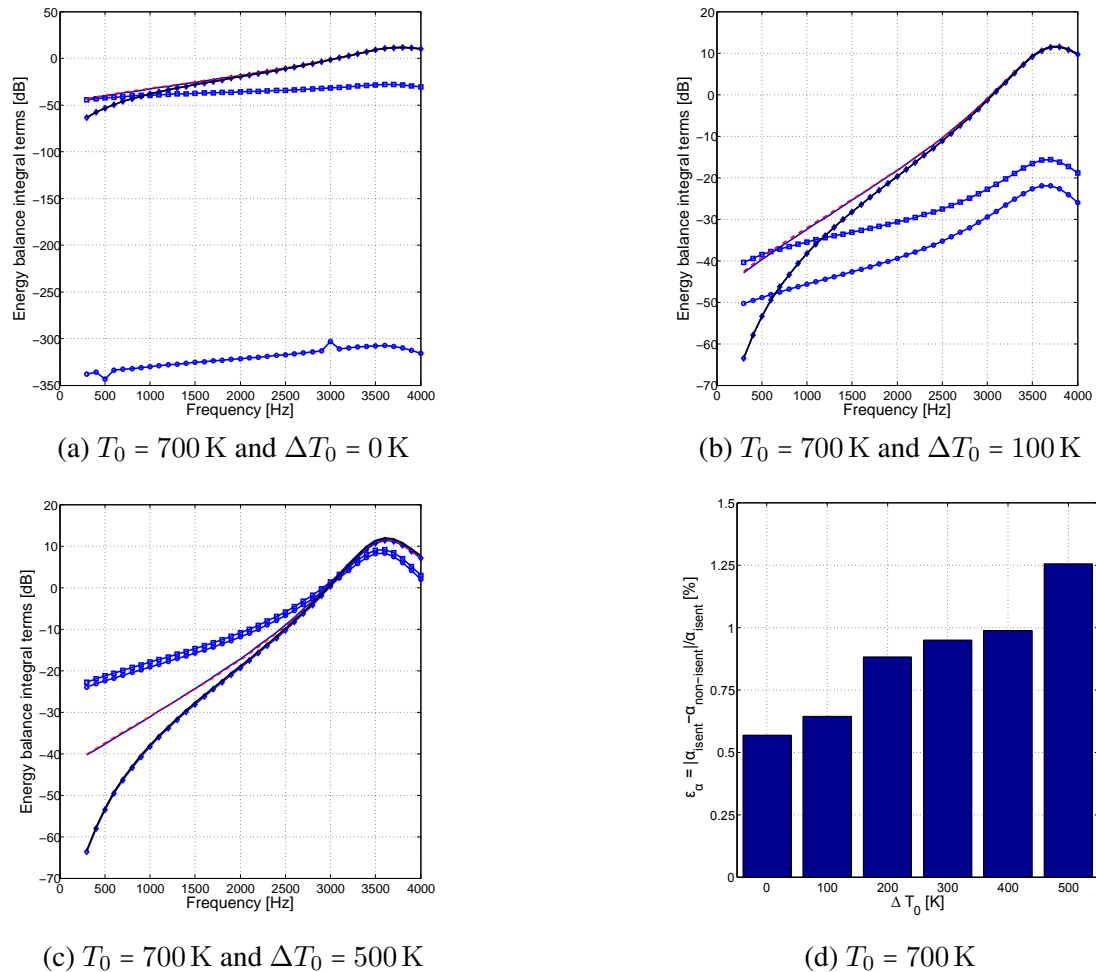
(d) $T_0 = 700\,\mathrm{K}$

Figure 5: (a)(b)(c) Evaluation of the integral terms defined in Eq.(4) for the energy balance over the computational domain from the non-isentropic set of LNS equations: total energy source $\mathbb{D}'$ (——), total energy flux $\mathbb{W}'$ (– – –), and the contributions of $\mathbb{D}'_v$ (—+—), $\mathbb{D}'_s$ (—o—), $\mathbb{D}'_\mu$ (—♦—), $\mathbb{D}'_{\dot{q}_V}$ (—✳—), and $\mathbb{D}'_t$ (—□—). $\mathbb{D}'$ obtained with simulations under isentropic assumption is also indicated (——). (d) Deviation in estimation of the peak magnitude of the absorption coefficient between the isentropic and non-isentropic p-FEM solvers, in function of the temperature gradient ΔT_0.

For $\Delta T_0 \neq 0$, it can be observed in Fig. 5(b) and Fig. 5(c) that the terms related to entropy $\mathbb{D}'_s$ and thermal diffusion $\mathbb{D}'_t$ increase significantly with ΔT_0. The range of frequencies for which these mechanisms are determinant is getting wider. It is also found that the term $\mathbb{D}'_s$ rises faster than $\mathbb{D}'_t$ for rising temperature gradients. In Fig. 5(c), $\mathbb{D}'_s$ and $\mathbb{D}'_t$ reach a similar order of magnitude. Overall, the peak amplitude of the total dissipation term $\mathbb{D}'$ varies very little with increasing ΔT_0, with an increase of the order of $1\,\mathrm{dB}$ from $\Delta T_0 = 0\,\mathrm{K}$ to $\Delta T_0 = 500\,\mathrm{K}$. This observation is actually the superposition of two opposite effects: an overall drop of the average temperature inside the orifice (which tends to decrease the dissipation) and an increasing temperature gradient (which contributes to enhance the dissipation).

As the entropy and thermal effects grow with increasing temperature gradient, the discrepancy between the results from the isentropic and non-isentropic solvers become larger with growing ΔT_0. This can be observed directly looking at the absorption coefficient α, as shown in Fig. 5(d). The relative deviation for the absorption coefficient ϵ_α between the two solvers is doubled for $\Delta T_0 = 500\,\mathrm{K}$ compared to the homogeneous condition. However, even if this discrepancy is increased with larger ΔT_0, the relative difference between the solvers is found to be small in the investigated cases, with $\epsilon_\alpha \leq 1.25\,\%$. From the detailed description of the dissipation mechanisms given in this study, it

is however to be expected that the deviation between the two solvers will increase significantly for acoustic resonators with lower resonance frequencies. This will be further investigated using the methodology described in the present work.

4. Conclusion

This paper investigates temperature and temperature gradient effects on the acoustic response of a Helmholtz resonator by using a FEM solution of the LNS equations. The numerical method showed to capture very well observations made experimentally. Compared to high-temperature experiments, the numerical approach allows a better control over the temperature field inside the resonator neck and the thorough investigation of the different mechanisms involved in the acoustic energy dissipation in presence of temperature gradients. For the present configuration and considered conditions, both isentropic and non-isentropic set of Linearized Navier-Stokes equations deliver similar results for the absorption peak amplitude, with a relative deviation of the order of 1%. However, the analysis of the different mechanisms involved in the dissipation of acoustic energy has shown that entropy and thermal effects become relevant in the low Helmholtz numbers range in presence of temperature gradients through the resonator neck. This is expected to be of importance for practical applications with Helmholtz resonators designed for a maximal damping at low frequency.

ACKNOWLEDGEMENTS

REFERENCES

1. Elnady, T., Bodén, H. and Kontio, T. Impedance of SDOF perforated liners at high temperatures, *Proceedings of the 10th AIAA/CEAS Aeroacoustics Conference*, Manchester, Great Britain, 10–12 May, (2004).

2. Wassmer, D., Còsìc, B. and Paschereit, C. O. Resonance frequency of Helmholtz dampers in the presence of high-temperature grazing flows, *Proceedings of the 20th AIAA/CEAS Aeroacoustics Conference*, Atlanta, Georgia, 16–20 June, (2014).

3. Bodén, H. and Kabral, R. The effect of high temperatures and grazing flow on the acoustic properties of liners, *Proceedings of the 10th European Congress and Exposition on Noise Control Engineering*, Maastricht, The Netherlands, May 31–June 3, (2015).

4. Bothien, M. R. and Wassmer, D. Impact of density discontinuities on the resonance frequency of Helmholtz resonators, *Journal of the American Institute of Aeronautics and Astronautics*, **53** (4), 877–887, (2015).

5. Denayer, H., Tournadre, J., De Roeck, W., Desmet, W. and Martínez-Lera, P. Combined numerical and experimental study of a slit resonator under grazing flow, *Proceedings of the 20th AIAA/CEAS Aeroacoustics Conference*, Atlanta, Georgia, 16–20 June, (2014).

6. Tournadre, J., Martínez-Lera, P. and Desmet, W. Numerical study of the acoustic response of a single orifice with turbulent mean flow, *Proceedings of the 22nd International Congress on Sound and Vibration*, Florence, Italy, 12–16 July, (2015).

7. Myers, M. K. Transport of energy by disturbances in arbitrary steady flows, *Journal of Fluid Mechanics*, **226**, 383–400, (1991).

8. Ullrich, W. C., Schulze, M. and Sattelmayer, T. Fundamental indirect noise generation by interactions between entropy, vorticity and acoustic waves in the context of aero engine applications, *Proceedings of the 43rd International Congress on Noise Control Engineering*, Melbourne, Australia, 16–19 November, (2014).

9. Maa, D.-Y. Microperforated panel wide-band absorber, *Noise Control Engineering Journal*, **29** (3), 77–84, (1987).

10. Allam, S. and Åbom, M. A new type of muffler based on microperforated tubes, *Journal of Vibration and Acoustics*, **133** (3), 8 pages, (2011).